PNAS
www.pnas.org

Supplementary Information for

Elucidating the native energy transfer dynamics of the purple bacteria peripheral antenna network

Dihao Wang, Olivia C. Fiebig, Dvir Harris, Hila Toporik, Chern Chuang, Yi Ji, Muath Nairat, Ashley L. Tong, John I. Ogren, Stephanie M. Hart, Jianshu Cao, James Sturgis, Yuval Mazor and Gabriela S. Schlau-Cohen

Gabriela S. Schlau-Cohen
E-mail: gssc@mit.edu

This PDF file includes:

Supporting Information Text

Materials and Methods

Preparation of LH2 and LH3. Wild-type *Ph. molischianum* DSM119 and DSM120 were provided by the Sturgis lab and grown as described previously with minor modifications(1). Briefly, 1000 mL of Hutner's media was degassed with nitrogen for one hour in a 1-L bottle, sealed with an open cap and silicone septum, and autoclaved for 20 min. Media was cooled to room temperature and inoculated with a live-growing bacterial culture. To produce LH2, the flask containing DSM119, which only produces LH2, was placed in front of a 70 W tungsten lamp, resulting in high-light and warm (30 ℃) temperature conditions. To produce LH3, the flask containing DSM120, which can produce both LH2 and LH3, was covered with a white paper napkin and further away from the tungsten lamp to create low-light and cool (23 ℃) temperature conditions. Several rounds of inoculating new culture were necessary for full conversion from production of LH2 to production of LH3. Purification was performed according to previous protocols (1, 2) using n-dodecyl-β-d-maltoside (DDM) as the detergent.

Preparation of ApoE422K Belting Protein and Lipids. The belting protein ApoE422K was used to produce doubly-loaded nanodisc samples. The plasmid (DNA 2.0) contained a thioredoxin fusion protein to improve belting protein expression, a thrombin cleavage sequence, a 6xHis tag, and kanamycin antibiotic resistance. A 10 mL starter culture of Luria Bertani Broth was inoculated with the glycerol stock and grown overnight in an incubator/shaker at 37 ℃, 180 rpm. The starter culture was used to inoculate 1 L of terrific broth. Protein overexpression was induced between 0.6 and 0.8 OD at 600 nm with a final concentration of 1 mM isopropyl-β-D-1-thiogalactopyranoside. Overexpression occurred for five hours. The cell pellet was collected by centrifuging for 20 min at 4000 rpm, 4 ℃and then resuspended in 25 mL of 20 mM Tris, 150 mM NaCl, 1 mM $MgCl_2$, pH 7.4 The following were added to the resuspension: phenylmethylsulfonyl fluoride to a final concentration of 1 mM, Triton X-100 to a final concentration of 0.1% v/v, and 10 μL (20 units) of DNase I (New England Biolabs). The solution was homogenized in a Dounce tissue homogenizer and then probe sonicated on ice for five minutes at 30% power, 30 seconds on and 30 seconds off. The lysate was centrifuged for one hour at 4000 rpm, 4 degrees C to remove cellular debris, and the supernatant was loaded onto a 25-mL Ni-NTA column. The column was allowed to equilibrate with the beads overnight on a nutating mixer at 4 C. Purification was carried out by washing with three column volumes each of 40 mM Tris HCl, 300 mM NaCl, 1% Triton-X 100, pH 8.0, 40 mM Tris HCl, 300 mM NaCl, 20 mM imidazole, 50 mM Na Cholate pH 8.0, 40 mM Tris HCl, 300 mM NaCl, 50 mM imidazole pH 8.0, 40 mM Tris HCl, 300 mM NaCl, 100 mM imidazole pH 8.0, and 40 mM Tris HCl, 300 mM NaCl, 400 mM imidazole pH 8.0. The fractions containing ApoE422K were combined and dialyzed in 1 L 20 mM Tris, 100 mM NaCl, 0.5 mM EDTA, pH 7.4 with three buffer changes every eight hours. 100 uL (1000 units) of TEV protease (New England Biolabs) were added to the sample and incubated overnight at 4 ℃on a nutating mixer to simultaneously cleave the histidine tag and the thioredoxin fusion protein. The TEV and cleaved fusion protein and histidine tag were removed by loading the sample on a 25-mL Ni-NTA column that was incubated overnight, ensuring that the cleaved fusion protein and histidine tag were bound to the column. The purified, cleaved ApoE422K was collected by washing the column with 20 mM Tris HCl, 150 mM NaCl, pH 7.4. The histidine tag and cleaved fusion protein were removed from the column by washing with 40 mM Tris HCl, 300 mM NaCl, 400 mM imidazole, pH 8.0.

The powdered form of 1,2-dimyristoyl-sn-glycero-3-phosphocholine (DMPC) was purchased from Avanti Polar lipids. A 100 mM stock solution was prepared by dissolving in 20 mM TrisHCl, 150 mM NaCl, 100 mM Na Cholate, pH 7.5 and sonicated in a bath for one hour. The stock solution was prepared fresh for each preparation of nanodiscs.

Assembly of Doubly-Loaded LH2 Nanodiscs. Nanodiscs loaded with LH2 and LH3 were produced using the belting protein ApoE422K, which is a 22 kDa fragment of apolipoprotein E4. DMPC was used as the lipid. ApoE422K, LH2, LH3, and DMPC were mixed together in a ratio of 1:0.125:0.125:22.2. This ratio was chosen to maximize the number of doubly-loaded discs produced, as at this ratio theoretically 100% of discs produced would contain two proteins in order to minimize the number of discs that only contained one protein. The reaction mixture was produced by adding each of the following in this order: lipid (DMPC), LH2, LH3, buffer (20 mM Tris HCl, 150 mM NaCl, pH 7.5), protease inhibitor cocktail (5 μL), and belting protein (ApoE422K). The belting protein was added last to prevent premature formation of nanodiscs. The reaction was incubated on a rocker for one hour at room temperature. Bio-Beads SM-2 Resin (Bio-Rad Laboratories) were added to 2/3 the volume of the reaction and incubated on a rocker for five hours at room temperature and then overnight at 4 ℃.

The nanodiscs were purified by fast protein liquid chromatography (FPLC) on a BioRad NGC Chromatography system (Bio-Rad Laboratories) on a Superdex 200 Increase 10/300 GL (Cytiva). The flow rate was 0.4 mL/min and the buffer used was 20 mM Tris HCl, 150 mM NaCl, pH 7.5. The FPLC peaks were characterized by linear absorption, SDS-PAGE, and transmission electron microscopy (TEM) to identify the fractions that contained LH2-LH3 nanodiscs.

nsTEM Sample Preparation and Measurements. Nanodisc samples were prepared for TEM on negatively glow-discharged 400-mesh Cu–carbon coated films (Electron Microscopy Sciences). 5 μL of sample was deposited onto the grid for one minute and then excess removed using Whatman filter paper. 5 μL of a 2% (w/v) uranyl acetate solution in water was added to the grid for 30 seconds and excess stain removed. Samples were allowed to air dry for at least one hour before imaged on a FEI Tecnai (G2 Spirit TWIN) at 120 kV at the MIT Materials Research Laboratory (MRL) Shared Experimental Facilities. The distribution of disc sizes was determined via ImageJ software (https://imagej.nih.gov).

Sample preparation for single-particle cryo-EM analysis. Calculation of the correct concentration of membrane-discs for Cryo-EM was done as follows. LH2-LH3 are 88,303 Da. ApoE422K is 21,943 Da A single DMPC lipid is 678 Da. The ratio of membrane-disc components determined by optimization of membrane-disc reactions is 2 light harvesting complexes, 6 ApoE422K, and 120 DMPC which amount to a total weight of 389,614 Da. Concentration of discs was found by identifying the concentration of LH2 by the absorption of the B850 band. That concentration and the molecular weight of the whole disc were used to find the membrane-disc concentration in mg/mL. A disc concentration of 0.75 to 1 mg/mL was optimal for data collection. The sample was deposited on a gold standard R 1.2/1.3 holey carbon grids 300 mesh (Quantifoil) and vitrified by flash-plunging the grid into liquid ethane using an automated plunge freezer, a Vitrobot MarkIV (ThermoFisher/FEI) with a blotting time of 5 s and a blot force of 5.

CryoEM data acquisition and processing. The cryo-EM specimens were imaged on a Titan Krios transmission electron microscope (ThermoFisher/FEI). Electron images were recorded using a Falcon III direct electron detect camera (FEI) at super-resolution counting mode. The nominal magnification was ×92,000, corresponding to a super-resolution pixel size of 0.1599 Å at the specimen level. The counting rate was adjusted to 19.37 e^-/px/s. Total exposure time was 7.00s, accumulating to a dose of 54.56 $e^-/Å^2$.

Data processing was carried out with Relion 3.0 suite (3). Relion implementation of MotionCorr was used to register the translation of each sub-frame. Contrast transfer function parameters for each movie were determined using CTFFIND4(4). Autopicking using LoG resulted in 1706944 particles, which where then 2D classified in an unsupervised manner, without alignment. Of those, 366361 particles clustered into 23 classes, which were then picked to either the parallel or the anti-parallel cascades. 3D reconstruction of anti-parallel and parallel reference maps were used to preform 3D classification. This procedure yielded classes which clearly showed the parallel (59893 particles) and anti-parallel (105458 particles) orientations. Several further rounds of 2D classification resulted in the final sets which contained 28771 parallel and 71566 anti-parallel particles. Three-dimensional reconstructions of parallel and anti-parallel orientations using these sets yielded volumes at a resolution of 10.8Å and 6.8Å, respectively. Lastly, high-resolution crystal structures of *Ph. molischianum* LH2 (PDB Code 1LGH) and an I-TASSER (5) homology model of LH3 based on *Rh. acidophilus* LH3 (PDB Code 1IJD) were docked into the densities using ChimeraX fit-in-map function.

Steady-State and Lifetime Measurements. Linear absorption spectra were recorded using an Epoch microplate spectrophotometer (BioTek) on the purified nanodisc samples. The absorption measurements were repeated after the TA experiments to confirm the absence of any sample degradation. The steady-state fluorescence measurements were taken using a home-built fluorescence setup with 532 nm excitation, an 800 nm 150 g/mm grating, and a PIXIS CCD camera (Princeton Instruments) (6). The fluorescence lifetime measurements were carried out using time-correlated single-photon counting (TCSPC) and fit as described previously (1, 2). The excitation wavelength was selected with a 790 nm 10-nm bandpass filter (FB790-10, Thorlabs, NJ). The emission wavelength was selected with an 860 nm longpass filter (FB860-10, Thorlabs, NJ). The excitation density was 10 $\mu W/cm^2$. The instrument response function (IRF) was 76 ps.

Sample Preparation for Ultrafast Spectroscopy. After purification, the nanodiscs were diluted to ∼1.5 OD at a 1 cm path length at 850 nm for doubly-loaded and singly-loaded nanodiscs containing LH2 and at 820 nm for singly-loaded nanodiscs containing LH3 in 20 mM Tris, 150 mM NaCl, pH 7.4. Power dependence was previously performed to confirm all experiments were conducted in the linear regime. The sample was flowed using a peristaltic pump and stored on ice during data acquisition. Linear absorbance spectra of all samples were acquired pre- and post-acquisition to monitor for degradation.

Transient Absorption Spectroscopy. The transient absorption (TA) setup consists of a regeneratively amplified Ti:Sapphire laser (Libra, Coherent, Santa Clara, CA) producing femtosecond pulses centered around 800 nm at a repetition rate of 5 kHz. The output was split into two arms, one arm was used directly as the pump and the other arm was sent into an Ar-filled tube to generate a white-light continuum. The white-light arm was used as a probe after it was spectrally filtered between 700-900 nm and compressed using a pair of prisms. The pump arm was modulated at 2.5 kHz using an optically-gated chopper and then sent into an optical delay line and a half-wave plate to set its relative polarization at magic angle. Neutral density filters were used to set the pump and probe energies to 40 and 0.4 nJ/pulse, respectively. Both arms were non-collinearly combined and focused using achromatic lenses with a 30.0 cm focal length into a flow cuvette with a 1 mm optical path. The probe arm was collected using a home-built Czerny-Turner spectrograph and was detected with a CCD array (Aviiva EM2, Teleydyne e2v) on a shot-to-shot basis. Each two consecutive laser shots were used to calculate the TA spectrum at each delay point using $\Delta TA = \log(\text{pump off/pump on})$. For each scan, 2500 TA spectra were collected at each time delay across the TA trace and further traces were repeated and averaged until good signal-to-noise traces were obtained. Global and Target analysis for the TA data was carried out using Glotaran software (7).

Kinetic Models and Data Analysis. The reaction schemes for LH2 and LH3 DLD samples are shown in Fig. S7. In detergent-solubilized samples, the pump pulse at 800 nm directly excites B800 ring. The excited-state lifetime was measured by TCSPC and fixed to be 1 ns (k_5=0.001 ps^{-1}) in the TA data analysis. The energy is then transferred to the B820 in LH3 or B850 ring in LH2. The dynamics of each elementary step can be obtained by following equations according to the scheme for LH3 DLD:

$$\frac{d[B800_{LH3}]}{dt} = -k_1 \frac{d[B800_{LH3}]}{dt} \quad [1]$$

$$\frac{d[B820]}{dt} = -k_3\frac{d[B820]}{dt} + k_1\frac{d[B800_{LH3}]}{dt} \quad [2]$$

$$\frac{d[B820^{rel}]}{dt} = -k_5\frac{d[B820^{rel}]}{dt} + k_3\frac{d[B820]}{dt} \quad [3]$$

and for LH2 DLD:

$$\frac{d[B800_{LH2}]}{dt} = -k_2\frac{d[B800_{LH2}]}{dt} \quad [4]$$

$$\frac{d[B850]}{dt} = -k_4\frac{d[B850]}{dt} + k_2\frac{d[B800_{LH2}]}{dt} \quad [5]$$

$$\frac{d[B850^{rel}]}{dt} = -k_5\frac{d[B850^{rel}]}{dt} + k_4\frac{d[B850]}{dt} \quad [6]$$

The LH3-LH2 DLD sample contains three subpopulations of LH2-LH2, LH3-LH2 and LH3-LH3 DLDs. The extinction coefficients of LH2 and LH3 at 800 nm are 2300 and 3300 $mM^{-1}cm^{-1}$, respectively. Based on the excitation coefficients and laser conditions, we derived the excited population ratios in our mixture sample. With the knowledge of SADS from previous fitting results, the dynamics of energy transfer from LH3 to LH2 can be solved by fitting the following equations:

$$\frac{d[B800_{LH3}]}{dt} = -k_1\frac{d[B800_{LH3}]}{dt} \quad [7]$$

$$\frac{d[B820]}{dt} = -k_3\frac{d[B820]}{dt} - k_5\frac{d[B820]}{dt} + k_1\frac{d[B800_{LH3}]}{dt} \quad [8]$$

$$\frac{d[B850]}{dt} = -k_4\frac{d[B850]}{dt} + k_3\frac{d[B820]}{dt} + k_2\frac{d[B800_{LH2}]}{dt} \quad [9]$$

$$\frac{d[B850^{rel}]}{dt} = -k_5\frac{d[B850^{rel}]}{dt} + k_4\frac{d[B850]}{dt} \quad [10]$$

Theoretical Calculation Models and Methods. In this section we introduce the models accounting for the excitonic structure of LH2/LH3, as well as the generalized FRET formalism adopted to calculate the inter-complex excited state energy transfer rates.

Frenkel Exciton Models. We aim at building a Frenkel exciton model for the B800-850 pigment protein complexes (LH2) from *Phaeosprillum molischianum* and that of the blue-shifted B800-820 complexes from the same organism grown under stress (LH3). Both of these complexes are octameric. We base the models on the parametrization by Chmeliov et al.,(8) where a different purple bacterium, *Rhodoblastus acidophilus*, with nonameric LH2 and LH3 complexes were studied. Specifically, we adopt the on-site energies and the short-range coupling terms from this model, and long-range (second neighbors and farther) couplings are calculated using transition monopole approximation(9, 10) based on the cryoEM structure. The transition charges corresponding to the ground and the first excited state (Q_y transition) of the BChl molecules are calculated using the ZINDO method implemented in Gaussian.(11) The numerical values for the on-site energies and the couplings are listed in Tables S3 and S4.

The inter-complex couplings are also calculated using the transition monopole approximation, explicitly:

$$J_{12} = \sum_{i,j}\frac{q_i^{(1)}q_j^{(2)}}{\epsilon|\vec{r}_i^{(1)} - \vec{r}_j^{(2)}|} \quad [11]$$

where i (j) runs over all atoms of molecule 1 (2), q_i and $\vec{r}_i$ are the transition monopole and the position of the corresponding atoms, and ϵ is the vacuum permittivity. The values for transition monopoles are for the Q_y transition of BChl and are available upon reasonable request.

Generalized FRET Rate. To account for the near-field effect in estimating the excitonic energy transfer rate between two adjacent complexes, we adopt the generalized FRET formalism.(12, 13) Here the energy transfer rate between a group of donor molecules, collectively excited in their one-exciton manifold, and a group of a acceptor molecules is expressed as

$$k_{\mathrm{ad}} = \frac{1}{2\pi\hbar^2}\int_{-\infty}^{\infty} dt \cdot \mathrm{Tr}[\mathbf{J}^T\mathbf{E}^{(\mathrm{d})}(t)\mathbf{J}\mathbf{A}^{(\mathrm{a})}(t)] \quad [12]$$

where $\mathbf{J} = \sum_{m=1}^{N_\mathrm{d}}\sum_{n=1}^{N_\mathrm{a}}|m\rangle\langle n|J_{mn}$ is the matrix containing pairwise excitonic couplings between all N_d donor and N_a acceptor molecules. $\mathbf{E}^{(\mathrm{d})}(t)$ and $\mathbf{A}^{(\mathrm{a})}(t)$ are the matrices of the emission and absorption operators of the donor and acceptor molecules

in the time domain, respectively. We refer the reader to ref.(13) for details. Further assuming the diagonal approximation in the energy eigenbasis, we arrive at

$$k_{\rm ad} \approx \frac{1}{2\pi\hbar^2} \sum_{\mu=1}^{N_{\rm d}} \sum_{\nu=1}^{N_{\rm a}} p_\mu(T) |J_{\mu\nu}|^2 \int_{-\infty}^{\infty} d\omega \cdot E_\mu(\omega) A_\nu(\omega) \qquad [13]$$

where $J_{\mu\nu}$ is the excitonic coupling matrix element between energy eigenstates μ of the donor group and ν of the acceptor group. $p_\mu(T) = e^{-\epsilon_\mu/k_{\rm B}T}/Z$ is the Boltzmann population of donor state μ and $Z = \sum_\mu e^{-\epsilon_\mu/k_{\rm B}T}$ is the partition function. $E_\mu(\omega)$ and $A_\nu(\omega)$ are the lineshape functions of the corresponding states. This approximation is appropriate when the temperature is high such that the contributions from inter-state coherence terms is weak.

In our simulations we further assume a shifted Gaussian profile for the lineshape functions:

$$E_\mu(\omega) = \frac{1}{\sqrt{2\pi\sigma_\mu^2}} \exp\left(-\frac{(\omega - \omega_\mu + \lambda_\mu)^2}{2\sigma_\mu^2}\right) \qquad [14]$$

$$A_\nu(\omega) = \frac{1}{\sqrt{2\pi\sigma_\nu^2}} \exp\left(-\frac{(\omega - \omega_\nu - \lambda_\nu)^2}{2\sigma_\nu^2}\right) \qquad [15]$$

where ω_μ is the energy, σ_μ is the linewidth, and λ_μ is the reorganization energy of state μ. While the former is obtained from diagonalizing the Frenkel exciton Hamiltonian discussed in the previous section, the latter two are fitted from experimental spectra. Specifically, we assume a uniform reorganization energy for all states, $\lambda_\mu = \lambda_\nu = \lambda = 116$ ($\rm cm^{-1}$), and the spectral widths for the B800 band and those of the B820/B850 band are set to $\sigma_{\rm B800} = 241$ and $\sigma_{\rm B820} = \sigma_{\rm B850} = 301$ ($\rm cm^{-1}$), respectively.

The calculated energy transfer rates between two neighboring complexes in the parallel and the anti-parallel configurations, revealed by the cryoEM measurement, are tabulated in Table S5, where all rates are normalized with respect to the symmetric LH2-to-LH2 rate.

Distance Dependent Energy Transfer Rate. In this section we examine the dependence of the inter-complex energy transfer rate on the separation between the complexes. The results are shown in Fig.**??**. All rates irrespective of the underlying excitonic structures scale as R^{-6} as predicted by the Förster theory.

$$k_{\rm ad}^{\rm (F)}(R_{\rm ad}) \propto p_{\rm d} \kappa_{\rm ad}^2 S_{\rm ad} \frac{|\vec{\mu}_{\rm d}|^2 |\vec{\mu}_{\rm a}|^2}{R_{\rm ad}^6} \qquad [16]$$

where $p_{\rm d}$ is the donor population, $\kappa_{\rm ad} = \hat{\mu}_{\rm a} \cdot \hat{\mu}_{\rm d} - 3(\hat{\mu}_{\rm a} \cdot \hat{R}_{\rm ad})(\hat{\mu}_{\rm d} \cdot \hat{R}_{\rm ad})$ is the orientation factor, $S_{\rm ad}$ is the spectral overlap, and $\vec{\mu}_{\rm a}$, $\vec{\mu}_{\rm d}$ are the transition dipole moments. In the large separation limit, one simply substitutes the transition dipole moments with those of the far-field bright states of each complex and sets p_d to be that of the thermal population of the donor bright states.

On the other hand, notice the choice to use the separation between the closest inter-complex B820/B850 BChl pair instead of the center-to-center distance. This allows a more transparent visualization of the correct limit in the short-range regime. As such, the dominant contribution to the inter-complex rate is that between the closest pair of BChl molecules. Consequently, one also recovers the R^{-6} scaling in the limit. Here, in contrast to the large separation limit, we replace the transition dipole moments in Eq.(16) with those of the closest donor-acceptor pair, as well as the donor population with that on the single donor molecule.

It should be noted that the vertical gap between the R^{-6} scalings of the two limits reflects the effective number of pigments participating in the energy transfer process in the Förster picture. Assuming that both $\kappa_{\rm ad}$ and $S_{\rm ad}$ are similar in both the small- and the large-separation limits, the primary difference between the two limits comes from the magnitudes of the transition dipole moments and the donor population. For LH2 and LH3 complexes this amounts to a ratio of $10^2 - 10^3$ between the two limits.

In the intermediate regime, the rate dependence on separation is milder than the R^{-6} scaling of the two limits. This is a consequence of both the two limits and the vertical gap between them, as discussed in the last paragraph. It should be noted that in all cases the rates in the naturally occurring systems fall under this regime.

Exciton Transportation Simulation. We simulated the excitation energy transfer dynamics between LH2 complexes using a hexagonal lattice model. A random LH2 on the lattice was selected in each simulation run as the starting point. The exciton lifetime was set as 1 ns. We only consider the exciton hopping between neighboring LH2s, and the hopping probability was proportional to the energy transfer rates ($\rm ps^{-1}$) of different distances. Three membrane organizations of different intercomplex distances were investigated. First, the intercomplex distances (edge-to-edge) were set at 4 nm (uniform arrangement). Then, 7.7% of the intercomplex distances were set as 1 nm, while the rest remained 4 nm. These closely packed LH2s were either randomly distributed (random arrangement) or formed a central cluster (cluster arrangement) on the lattice. For each different arrangement, the exciton transportation distance was averaged over 30000 simulation runs. Furthermore, to cover all the possibilities, we examined the exciton hopping distances of 100 different random arrangements. The simulation results are shown in Table S6.

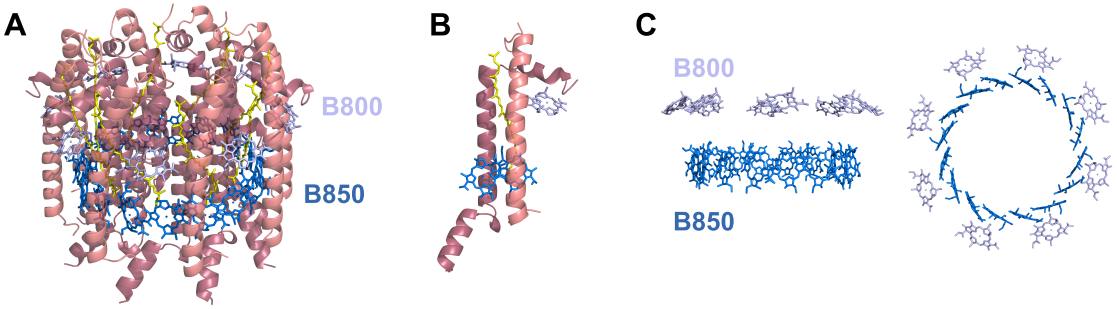

Fig. S1. Protein structure of (A) Light-harvesting Complex 2 in *Ph. molischianum* (Protein Data Bank ID code 1LGH) and the subunit (B). The LH2 complex consists of 8 subunits. Each subunit is a heterodimer containing one B800 BChla (light violet), two B820 BChlas (blue), and one carotenoid molecule (yellow). (C) Side and top views of the B800 and B850 Bchla rings.

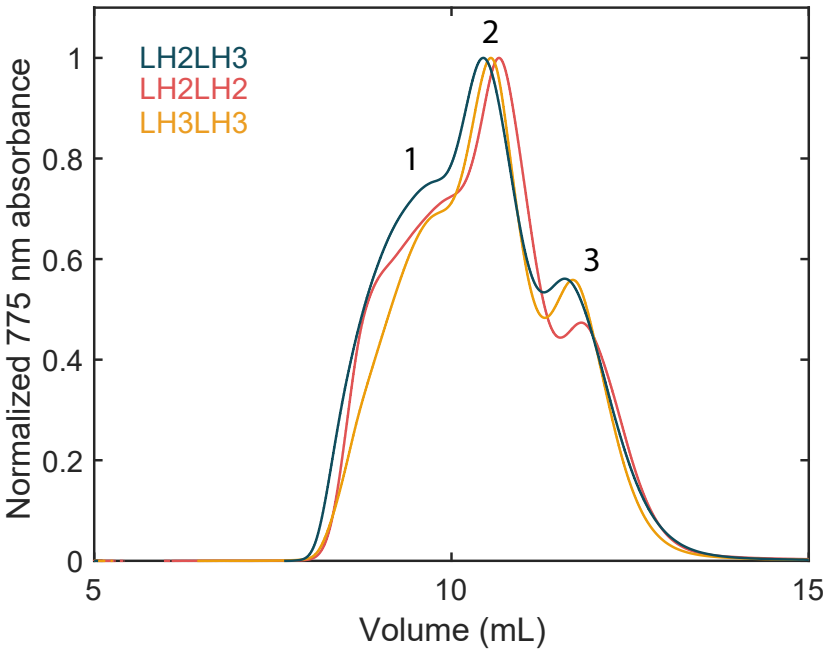

Fig. S2. Size-exclusion chromatography from FPLC of LH2 discs. Peak 1 contains larger aggregates and peak 2 contains DLDs. Peak 3 contains free LH2 and singly-loaded discs

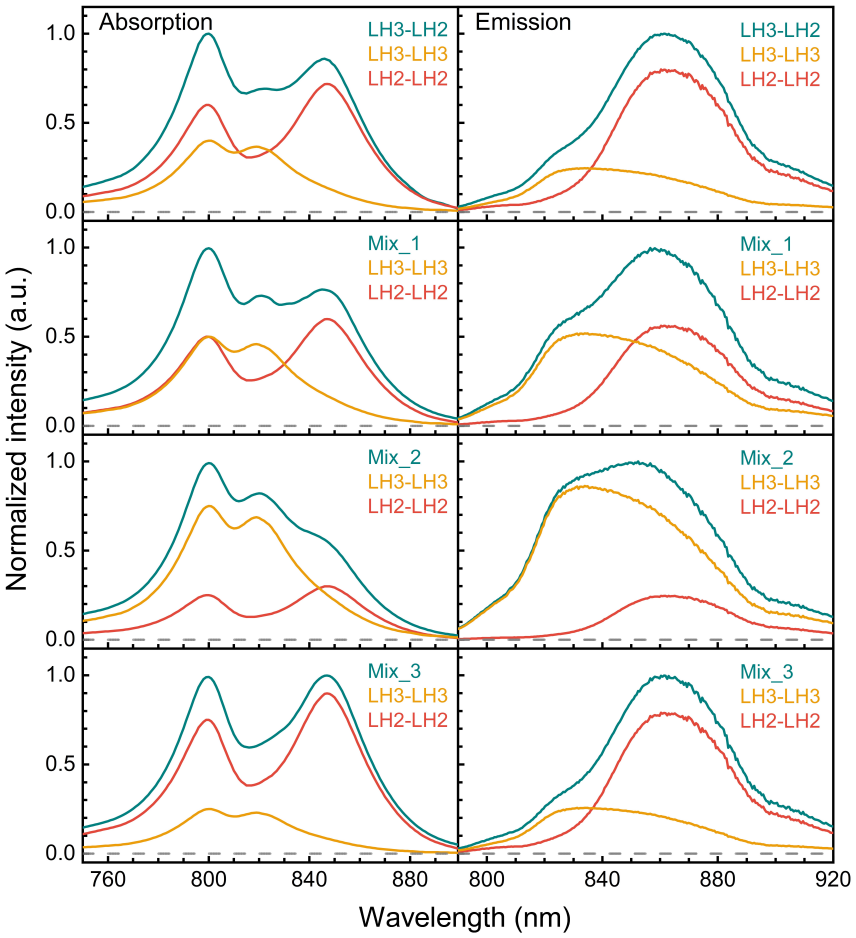

Fig. S3. Decomposition of steady-state absorption and emission spectra of LH3-LH2 DLD and three different mixtures of LH2-LH2 and LH3-LH3 samples.

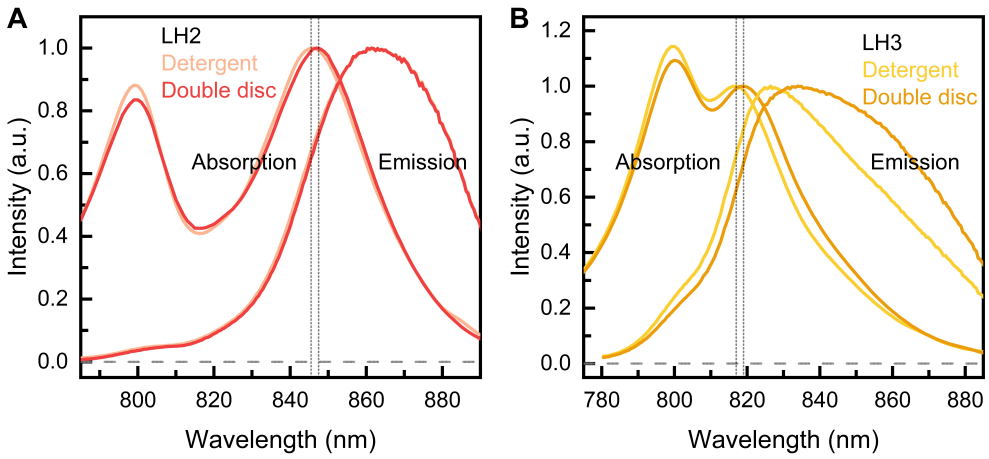

Fig. S4. Steady-state absorption and emission spectra of LH2 and LH3 in detergent and DLD. The steady-state absorption peaks are also shown with the dotted lines.

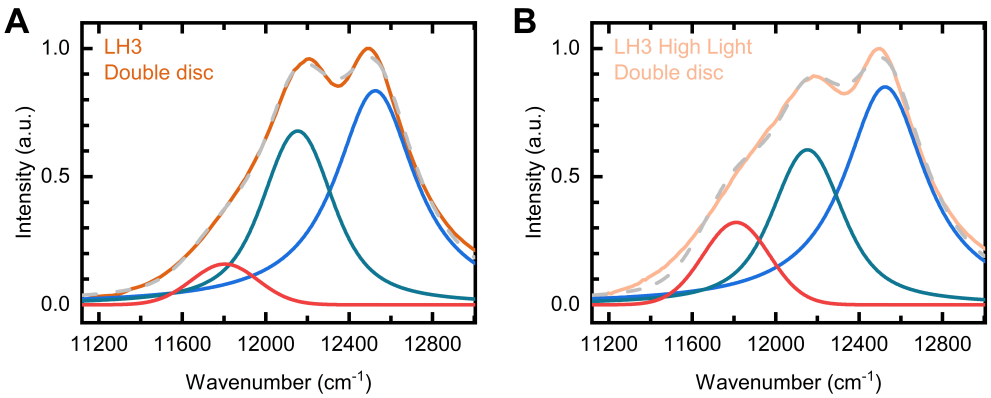

Fig. S5. Steady-state absorption spectra of LH3 (A) and LH3 under high light condition (B) in double discs. The absorption spectra are fitted with Voigt band shapes (gre dashed lines). The B800 fit is shown in blue, the B820 fit in dark cyan, and the B850 fit in red.

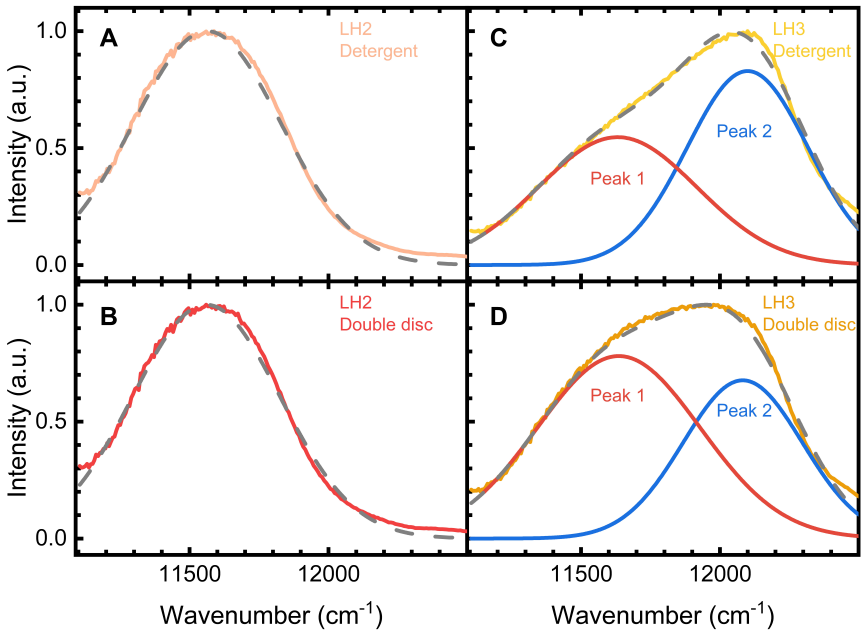

Fig. S6. Decomposition of LH2 and LH3 emission spectra in detergent (A, C) and DLD (B, D). The fitted spectra are shown with dashed lines (grey).

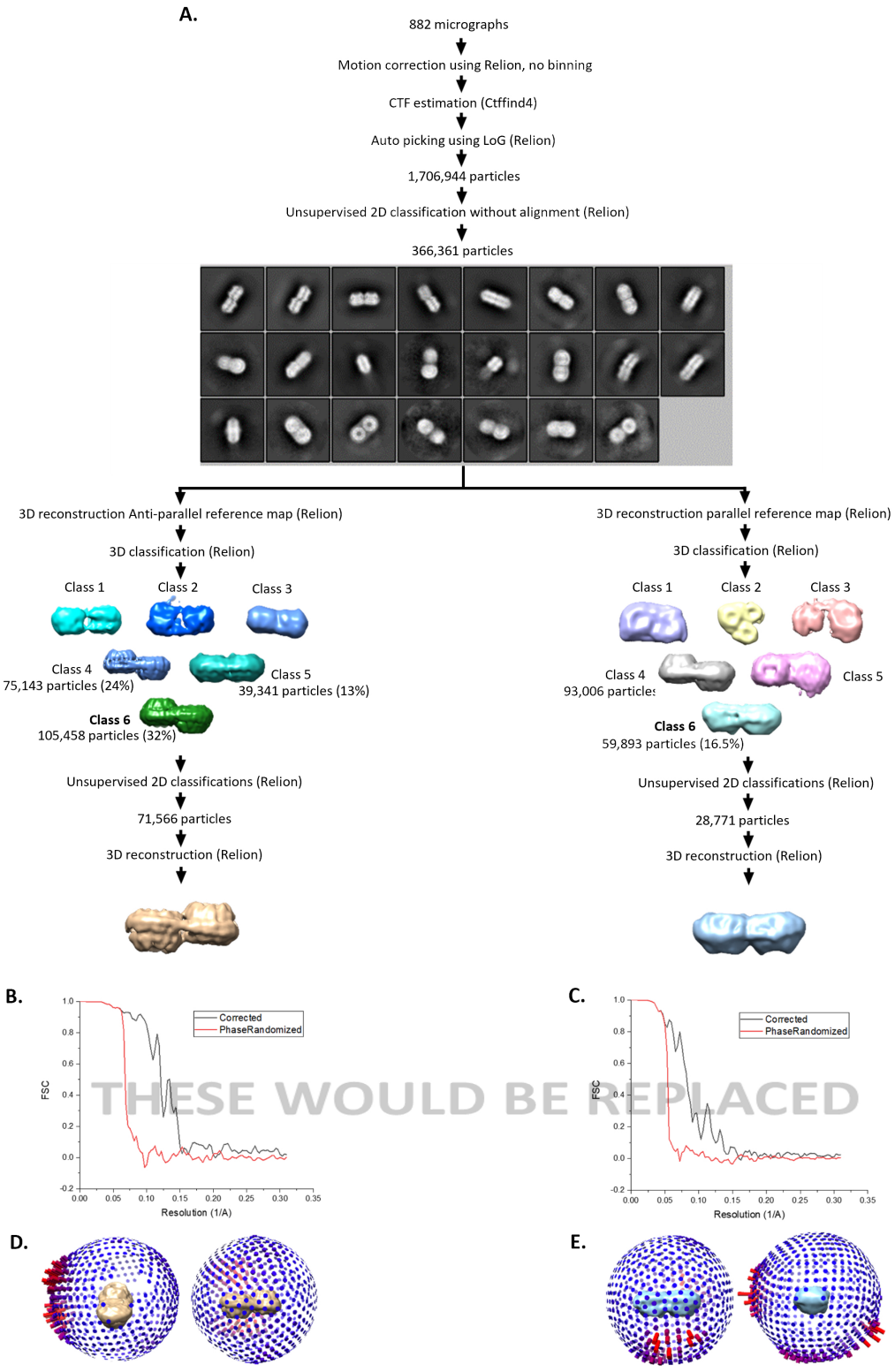

Fig. S7. CryoEM processing strategy. (A) Data collection and image processing strategy including selected 2D classes sorted by classes distribution and 3D classes. Further details can be found in the materials and methods section. (B) and (C) Plots of Fourier shell correlation (FSC) against resolution of the anti-parallel and parallel orientations, respectively. (D) and (E) Plots of Euler angle distribution of the anti-parallel and parallel orientations, respectively.

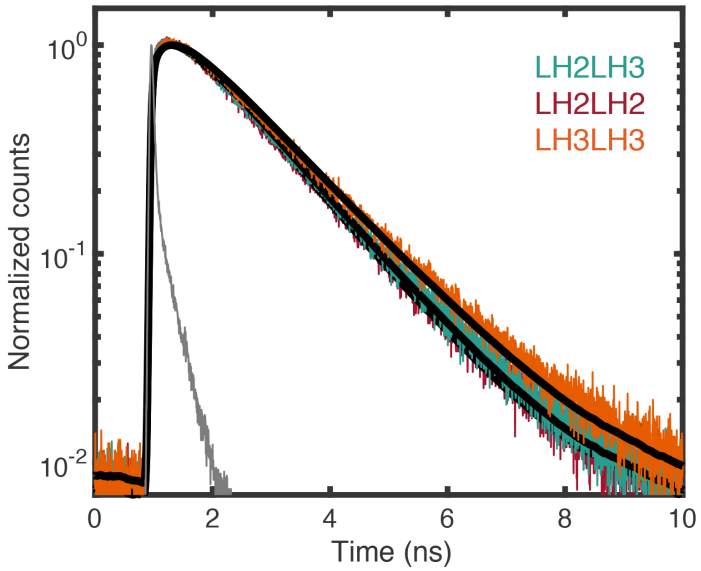

Fig. S8. Fluorescence decay transients at 860 nm for LH2-LH2, LH3-LH3, and LH2-LH3 DLD measured with time-correlated single photon counting.

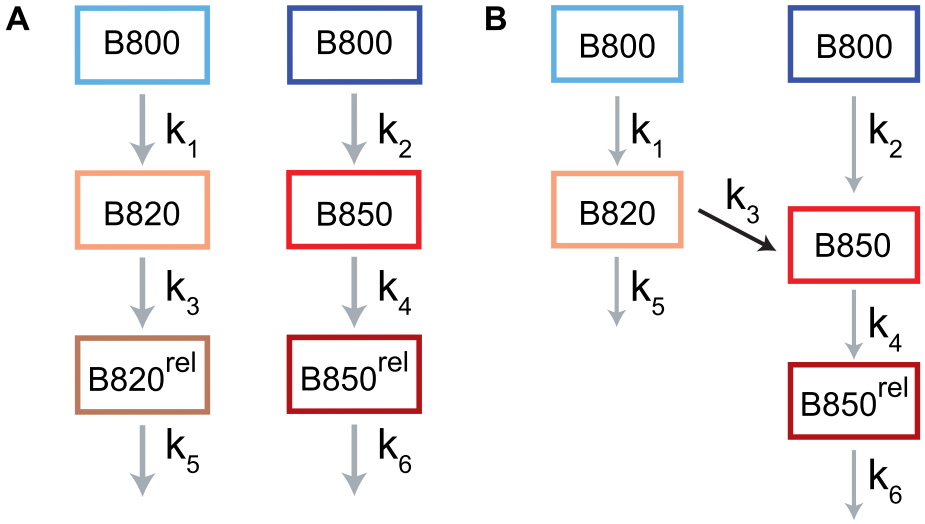

Fig. S9. Dynamic models of (A) LH2-LH2 and LH3-LH3 DLD and (B) LH3-LH2 DLD.

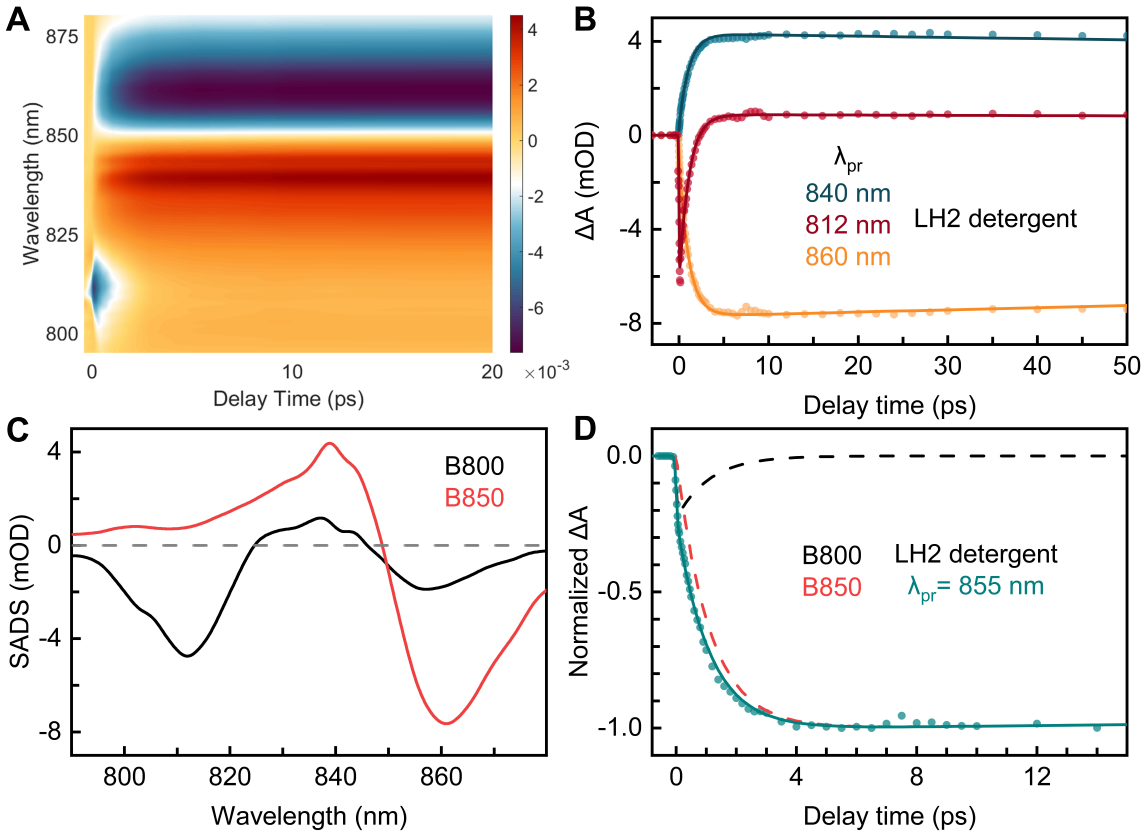

Fig. S10. (A) 2D representation of the femtosecond-resolved transient absorption spectra of LH2 in detergent (B) Absorption transients probed at typical wavelengths. All experimental data are shown as circles, and the solid lines are the best model fit. (C) SADS of B800 (black) and B850 (red). (D) Deconvolution of the transient probed at 855 nm into various dynamic components.

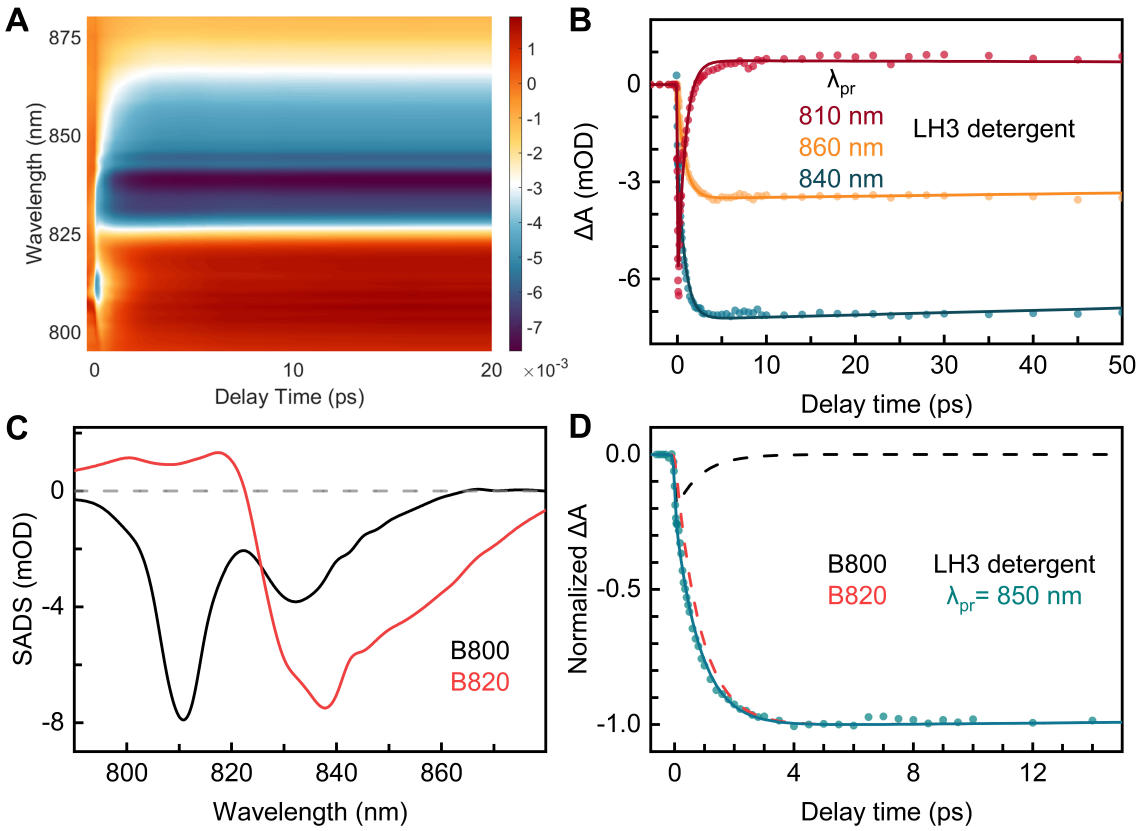

Fig. S11. (A) 2D representation of the femtosecond-resolved transient absorption spectra of LH3 in detergent (B) Absorption transients probed at typical wavelengths. All experimental data are shown as circles, and the solid lines are the best model fit. (C) SADS of B800 (black) and B820 (red). (D) Deconvolution of the transient probed at 850 nm into various dynamic components.

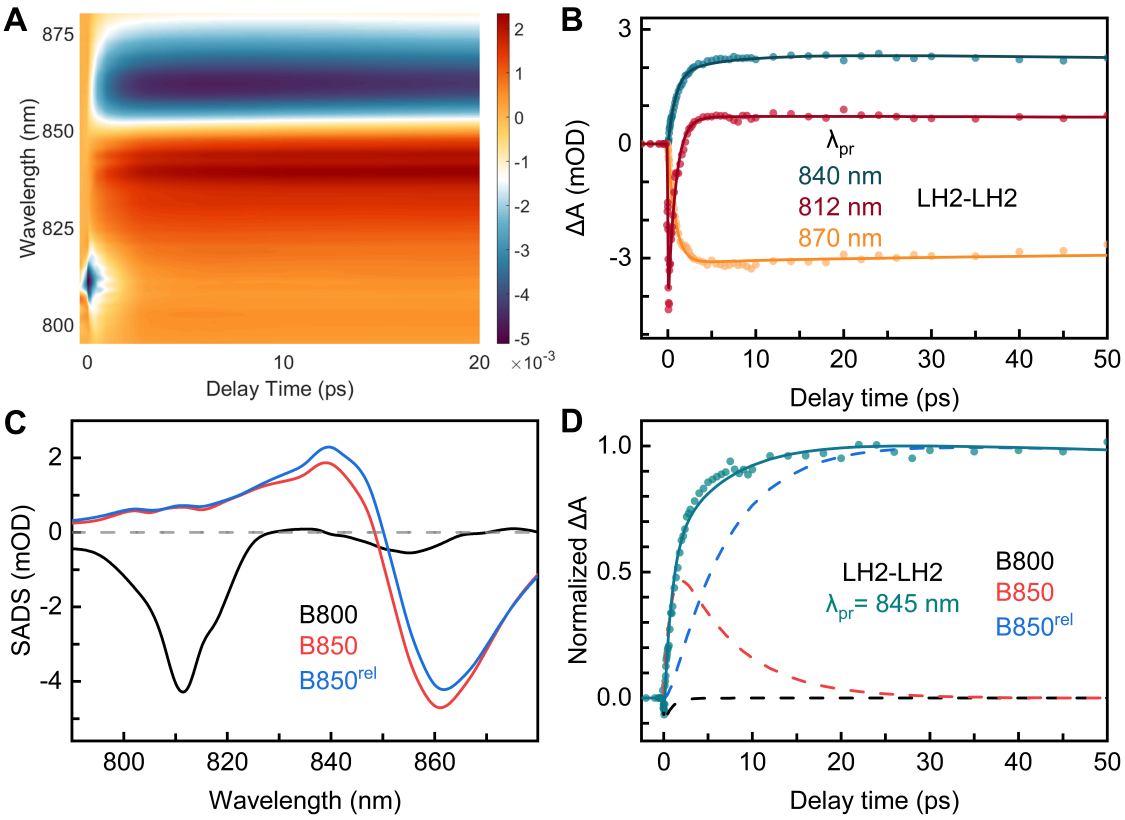

Fig. S12. (A) 2D representation of the femtosecond-resolved transient absorption spectra of LH2 DLD (B) Absorption transients probed at typical wavelengths. All experimental data are shown as circles, and the solid lines are the best model fit. (C) SADS of B800 (black), B850 (red), and $B850^{rel}$ (blue). (D) Deconvolution of the transient probed at 855 nm into various dynamic components.

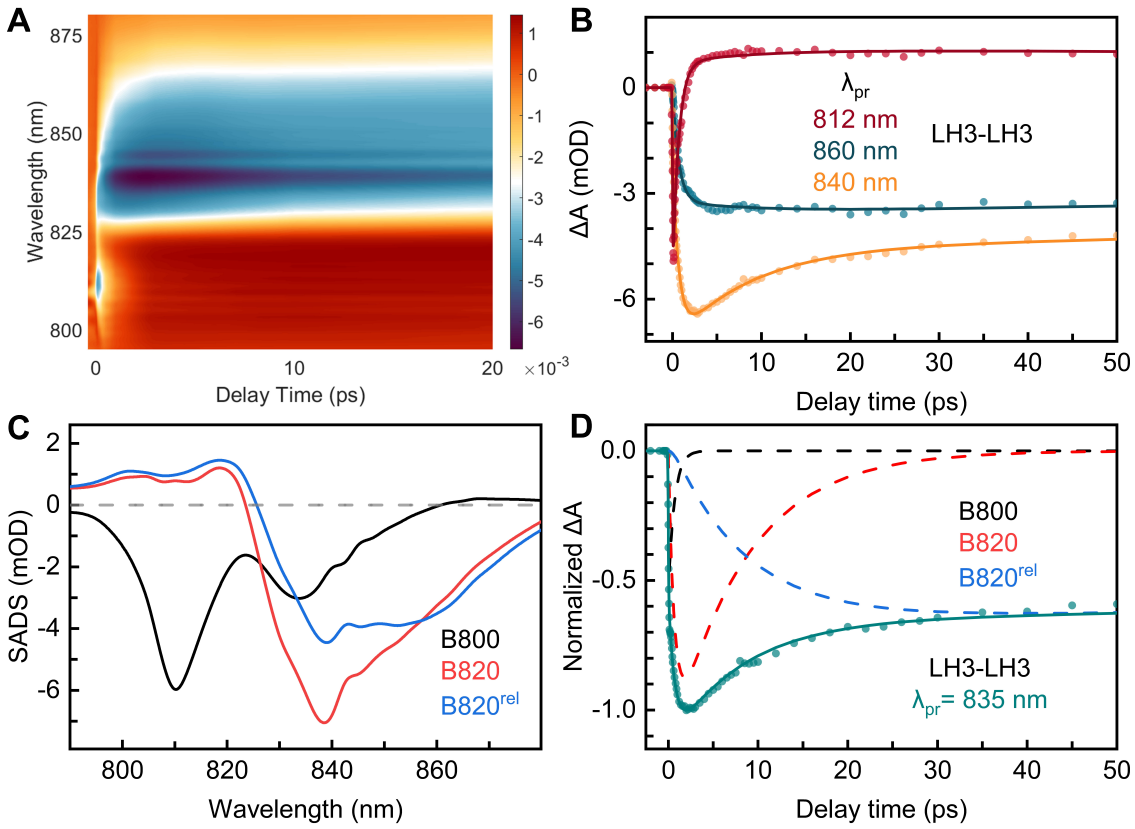

Fig. S13. (A) 2D representation of the femtosecond-resolved transient absorption spectra of LH3 DLD (B) Absorption transients probed at typical wavelengths. All experimental data are shown as circles, and the solid lines are the best model fit. (C) SADS of B800 (black), B820 (red), and $B820^{rel}$ (blue). (D) Deconvolution of the transient probed at 855 nm into various dynamic components.

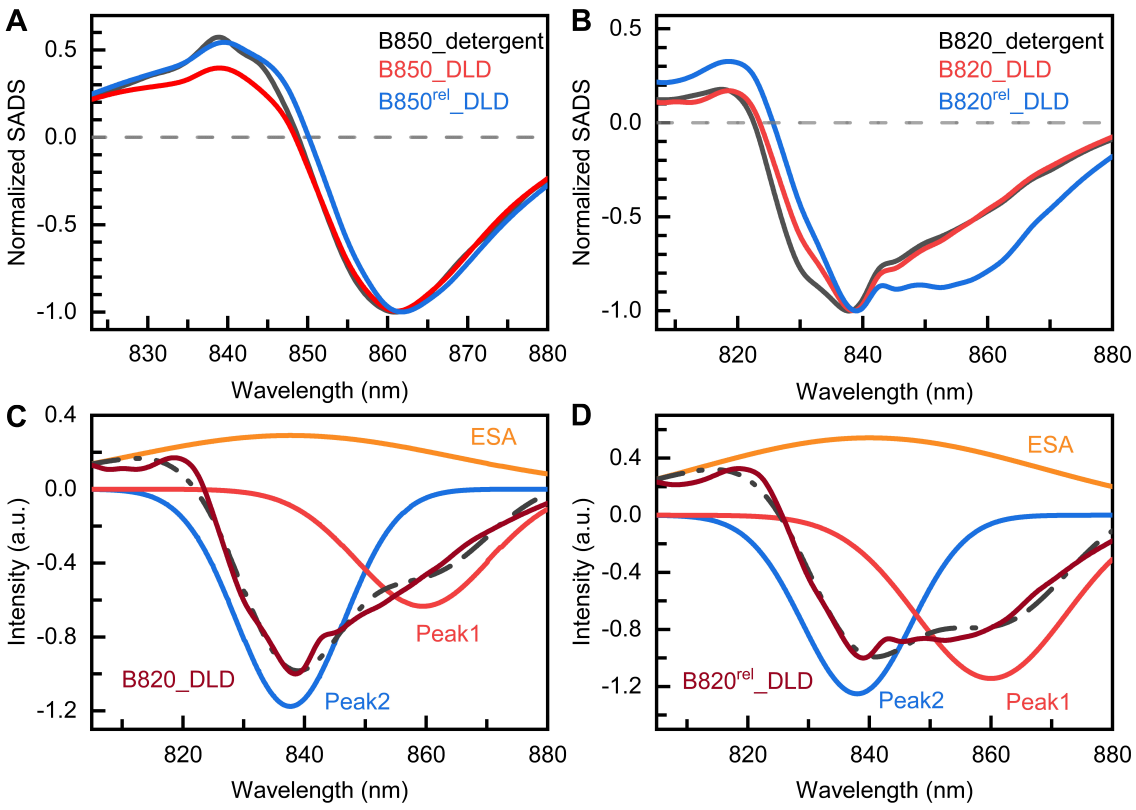

Fig. S14. Comparison of (A) B850 and (B) B820 SADS in detergent and DLD. SADS decomposition of (C) B820 and (D) $B820^{rel}$ into Gaussian peaks.

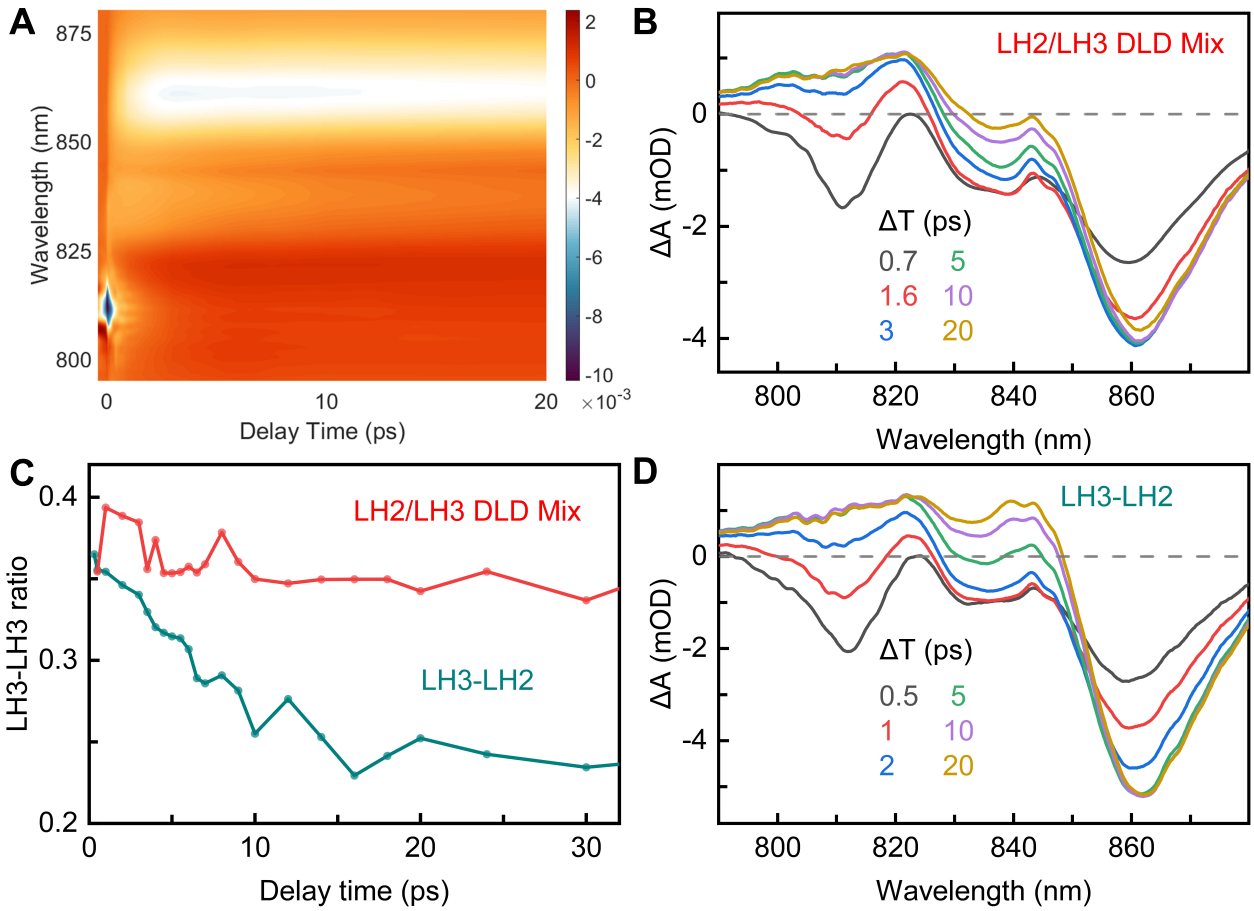

Fig. S15. (A) 2D representation of the femtosecond-resolved transient absorption spectra of the mixture of LH2-LH2 and LH3-LH3 DLD. (B, D) Transient-absorption spectra of the mixture and LH3-LH2 at typical time delays. (C) LH3-LH3 ratios from spectral decomposition. Note that the time-dependent ratio in LH3-LH2 reflects the population dynamics in the sample due to the energy transfer.

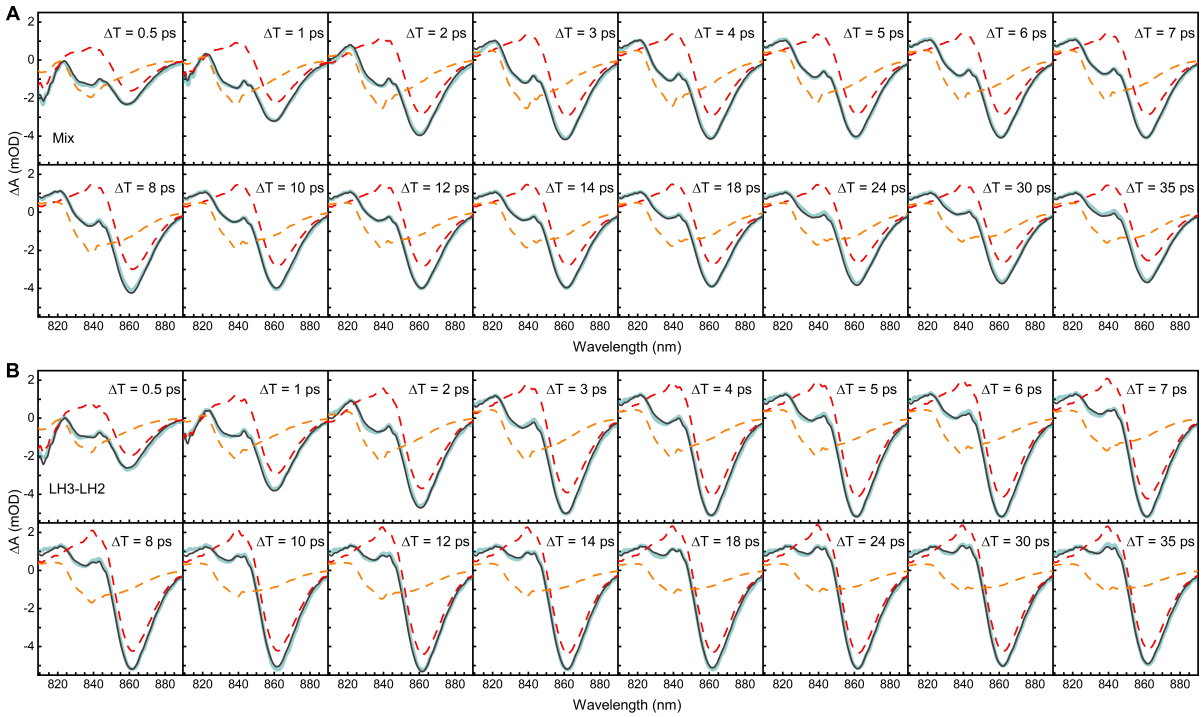

Fig. S16. Transient-absorption spectral decomposition of the (A) LH2-LH2 and LH3-LH3 mixture sample and the (B) LH3-LH2 DLD sample. The dashed lines show the corresponding LH2-LH2 (red) and LH3-LH3 (orange) spectra. The simulated spectra (solid grey line) are in good agreement with the measured spectra (shaded line, pale olive)

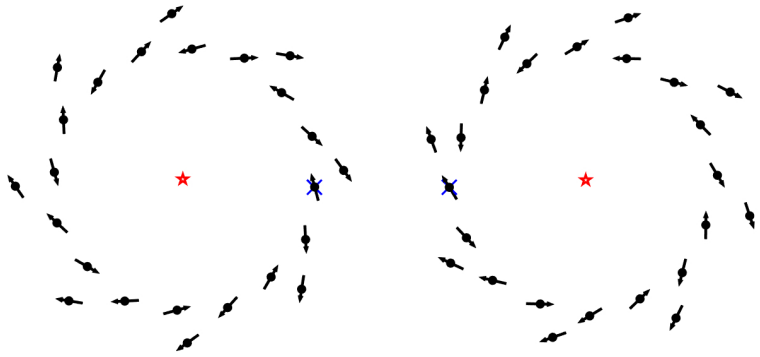

Fig. S17. The locations and dipole orientations of the BChl molecules in a parallel double ring configuration of the cryoEM structure, projected onto the xy-plane. The centers of the two rings are indicated by stars and the two BChl molecules on the B820/B850 rings that are the closest inter-complex pair are marked with crosses. The separation between them is 23.8 Å.

Table S1. Steady-state spectral peaks of LH3 and LH2 in detergent and DLD

Detergent	Absorption peak (nm)	Emission peak (nm)
B820	817	826
B850	846	862

DLD	Absorption peak (nm)	Emission peak (nm)
B820	819	834
B850	849	862

Table S2. Results of energy transfer dynamics of LH3 and LH2 in detergent and DLD

LH3	Tau1 (ps)	Tau3 (ps)	Tau5 (ns)
Detergent	0.84		1.7
DLD	0.68	8.1	1.4

LH2	Tau2 (ps)	Tau4 (ps)	Tau6 (ns)
Detergent	1.1		1.4
DLD	0.85	6.6	1.2

Table S3. On-site energies and intermolecular excitonic couplings for LH2 complexes in wavenumbers.

No.	B800	B850a	B850b
1	12524	-25	3
2	-18	4	19
3	-2	3	-2
4	0	1	-1
5	0	1	0
6	0	1	0
7	-2	2	-1
8	-18	3	-3
9	-25	12377	183
10	3	183	12004
11	3	-61	151
12	-3	16	-36
13	2	-7	12
14	-1	3	-4
15	1	-2	3
16	0	1	-1
17	1	-1	1
18	0	1	-1
19	1	-2	1
20	-1	3	-1
21	3	-7	3
22	-2	12	-4
23	4	-61	16
24	19	151	-36

Table S4. On-site energies and intermolecular excitonic couplings for LH3 complexes in wavenumbers.

No.	B800	B820a	B820b
1	12520	-25	3
2	-18	4	19
3	-2	3	-2
4	0	1	-1
5	0	1	0
6	0	1	0
7	-2	2	-1
8	-18	3	-3
9	-17	12602	162
10	2	161	12389
11	2	-40	92
12	-2	11	-24
13	1	-5	8
14	-1	2	-3
15	1	-2	2
16	0	1	-1
17	1	-1	1
18	0	1	0
19	1	-2	1
20	-1	2	-1
21	2	-5	2
22	-2	8	-3
23	3	-40	11
24	12	92	-24

Table S5. Relative energy transfer rates calculated with respect to the symmetric LH2→LH2 rate of the parallel configuration.

Relative Rate	Parallel	anti-parallel
LH2→LH2	1	0.97
LH3→LH2	1.46	1.43
LH3→LH3	1.54	1.68

Table S6. Transport distance of different LH2 arrangements.

Arrangement	Transport distance (nm)	Error (nm)
uniform	256	0
random	287.7210	0.1037
cluster	287.7210	0.1445

References

1. AL Tong, et al., Comparison of the energy transfer rates in structural and spectral variants of the b800-850 complex from purple bacteria. *The journal physical chemistry B* **124**, 1460–1469 (2020).
2. JI Ogren, et al., Impact of the lipid bilayer on energy transfer kinetics in the photosynthetic protein lh2. *Chem. science* **9**, 3095–3104 (2018).
3. J Zivanov, et al., New tools for automated high-resolution cryo-em structure determination in relion-3. *elife* **7**, e42166 (2018).
4. A Rohou, N Grigorieff, Ctffind4: Fast and accurate defocus estimation from electron micrographs. *J. structural biology* **192**, 216–221 (2015).
5. J Yang, et al., The i-tasser suite: protein structure and function prediction. *Nat. methods* **12**, 7–8 (2015).
6. L Wang, et al., Interfacial trap-assisted triplet generation in lead halide perovskite sensitized solid-state upconversion. *Adv. Mater.* p. 2100854 (2021).
7. JJ Snellenburg, SP Laptenok, R Seger, KM Mullen, IH van Stokkum, Glotaran: A java-based graphical user interface for the r package timp. (2012).
8. J Chmeliov, et al., Excitons in the LH3 complexes from purple bacteria. *J. Phys. Chem. B* **117**, 11058–11068 (2013).
9. K Sauer, KD Philipson, SC Tsai, Circular dichroism of chlorophyll and related molecules calculated using a point monopole model for the electronic transitions. *J. Phys. Chem.* **75**, 1440–1445 (1971).
10. JC Chang, Monopole effects on electronic excitation interactions between large molecules. i. application to energy transfer in chlorophylls. *J. Chem. Phys.* **67**, 3901–3909 (1977).
11. MJ Frisch, et al., Gaussian~16 Revision C.01 (2016) Gaussian Inc. Wallingford CT.
12. L Cleary, J Cao, Optimal thermal bath for robust excitation energy transfer in disordered light-harvesting complex 2 of purple bacteria. *New J. Phys.* **15**, 125030 (2013).
13. J Ma, J Cao, Förster resonance energy transfer, absorption and emission spectra in multichromophoric systems. I. Full cumulant expansions and system-bath entanglement. *J. Chem. Phys.* **142**, 094106 (2015).